Journal of
Applied Crystallography

ISSN 0021-8898

Received 5 August 2012
Accepted 7 November 2012

Advances in exploiting preferred orientation in the structure analysis of polycrystalline materials

Jürgen Grässlin,[a] Lynne B. McCusker,[a]* Christian Baerlocher,[a] Fabia Gozzo,[b] Bernd Schmitt[b] and Luca Lutterotti[c]

[a]Laboratory of Crystallography, ETH Zurich, Switzerland, [b]Swiss Light Source, PSI, Villigen, Switzerland, and [c]Department of Materials Engineering and Industrial Technology, University of Trento, Italy. Correspondence e-mail: lynne.mccusker@mat.ethz.ch

In an attempt to overcome the reflection overlap problem, which is the primary hindrance to structure determination from powder diffraction data, an experimental approach that exploits preferred orientation was developed some years ago. Now both the experimental setup and the data analysis procedure have been optimized, with the result that the quality of the extracted reflection intensities has been improved significantly and the synchrotron beamtime required for the data collection reduced. The one-dimensional Si microstrip detector Mythen II on the Materials Science beamline at the Swiss Light Source and new features in the data analysis software *MAUD* [Lutterotti, Matthies & Wenk (1999). *IUCr Commission on Powder Diffraction Newsletter*, No. 21, pp. 14–15] have made these improvements possible. The main changes in the experimental setup are (1) using an optimized set of sample orientations, (2) placing the detector such that both positive and negative 2θ angles are measured simultaneously, and (3) introducing an additional sample tilt angle, to measure data that cannot be accessed otherwise. On the data analysis side, the program *MAUD* is now used for both the determination of the orientation of the crystallites and the intensity extraction. The evaluation of data obtained from a textured zirconium phosphate pyridinium sample shows a significant improvement in the reliability of the structure factor amplitudes derived from overlapping reflections.

1. Introduction

Several ways of dealing with the reflection overlap problem in powder diffraction data have been developed in the past decade (Pecharsky & Zavalij, 2009). One of the few experimental approaches to the problem is the texture method, where an intentionally textured sample is measured at different sample orientations. The differences in the measured intensities can then be used to deduce the individual intensities of overlapping reflections. Hedel *et al.* (1997) showed that in theory, if a full texture analysis is performed, almost single-crystal-like data can be obtained. Since the first experimental tests using such a full texture analysis (Wessels, 1999), many changes in the experimental setup have been implemented.

The initial reflection mode experiment at the Swiss–Norwegian Beamline (SNBL) at the European Synchrotron Radiation Facility (ESRF) allowed the complex structure of the zeolite UTD-1F to be solved (Wessels *et al.*, 1999). However, there were a number of drawbacks, not the least of which was the enormous amount of beam time required (*ca* three days per sample). Further requirements included a relatively large homogeneously textured sample and a suitable material for calibration. Severe corrections for the sample tilt also had to be applied. Therefore, the experiment was redesigned. A transmission geometry setup using an imaging plate (Prokić, 2004) was implemented. With this geometry, a very small textured sample is bathed in the X-ray beam, so sample homogeneity is less of a problem, and the two-dimensional detector allowed more complete data sets to be collected in less time. However, the angular resolution (both in FWHM and $d_{\min}$) suffered. At the time, there were no area detectors with a sufficient number of pixels available to overcome this limitation, so a setup exploiting the one-dimensional Mythen I microstrip detector (Schmitt *et al.*, 2004) was devised (Massüger, 2007). Although this setup solved the resolution problems with only a modest increase in beamtime requirements, the limitations of the prototype detector made it difficult to obtain counting statistics good enough for reliable data analysis.

Now, with the advent of the Mythen II detector (Bergamaschi *et al.*, 2010), these problems have been solved. Fast measurements with good counting statistics, a large 2θ range and high resolution in peak width are now possible. By further modifying the experimental setup, the data collection strategy and the data analysis procedure (using *MAUD*; Lutterotti *et al.*, 1999), the method has been made more efficient and

reliable. All aspects have been evaluated using a zirconium phosphate pyridinium ($ZrPO_4$-pyr) (Dong *et al.*, 2007) test sample.

2. Data collection

2.1. Sample preparation

For this study, the textured samples were prepared using the bakery folding method (Wessels, 1999; Massüger, 2007) optimized by Estienne (2008). The sample powder (*ca* 0.02 g) was mixed with a few drops (300–500 µl) of tetrahydrofuran (C_4H_8O) in a mortar and dispersed with a pestle. The resulting suspension was then pipetted into a small tube and treated in an ultrasonic bath for a few minutes. One granule of polystyrene was added (approximate sample-to-polystyrene ratio of 1:2), and the tube was placed in the ultrasonic bath again until the polystyrene had dissolved completely. The mixture was then allowed to dry in a Teflon mold until it had reached the required gel-like viscosity. One drop of this gel mixture was put into a custom-made die with a 3 × 50 mm channel-shaped opening and pressed. The crystallites in the gel align along the flow direction. The die was then opened, and the sample folded and pressed again. This procedure was repeated several times until the resulting plate-like sample became too brittle. Finally, small pieces *ca* 0.3–0.4 mm in diameter were cut from this plate and examined with a single-crystal diffractometer to verify that an exploitable texture had been induced.

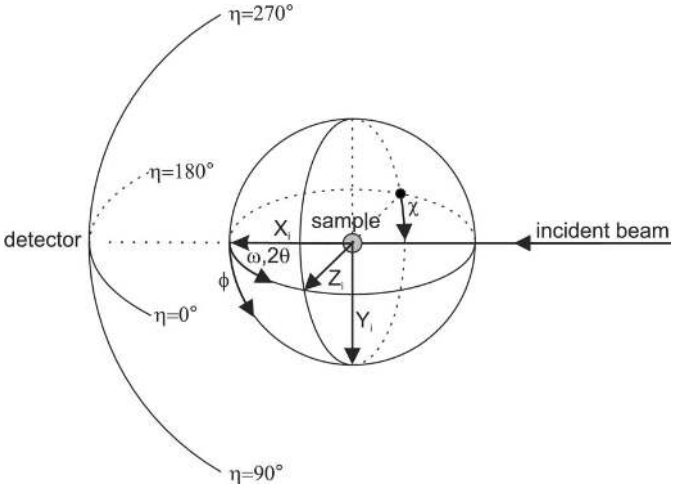

Figure 1
The *MAUD* angle convention for the setup at the SLS, showing the sample rotation (φ) and tilt (χ) angles, the detector orientation angle (η), and the diffraction angle (2θ) in the instrument coordinate system (X_i, Y_i, Z_i).

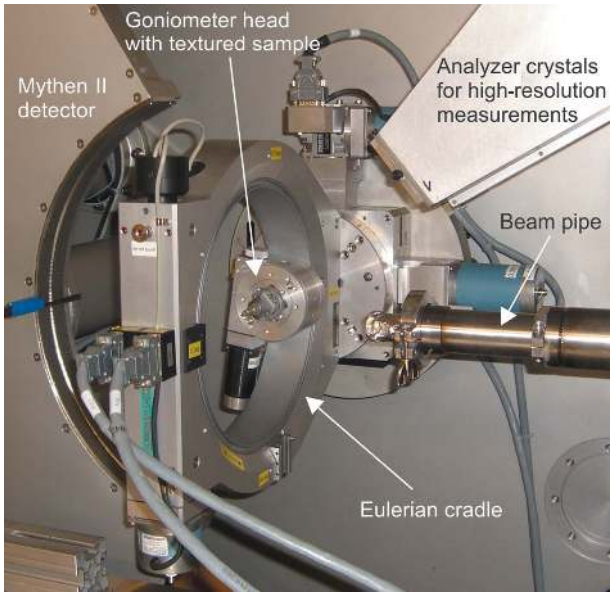

Figure 2
Photograph of the SLS experimental setup.

2.2. Experimental setup

A sketch with the *MAUD* angle convention that is used and a photograph of the transmission geometry setup on the Materials Science beamline at the Swiss Light Source (SLS) are shown in Figs. 1 and 2, respectively. The textured sample is mounted on a glass capillary that is fixed on a goniometer head. An Eulerian cradle is used to rotate (φ) and tilt (χ) the sample in the X-ray beam. At each orientation, the sample is oscillated around both φ and χ by 0.5° in order to illuminate more crystallites and thereby smooth the texture. Before the data collection, an untextured sample of cubic zeolite A (prepared in a polystyrene matrix but without bakery folding and mounted in the same way as the textured sample) is measured at different orientations φ/χ to ensure that the Eulerian cradle is well aligned and that the beam homogeneity is satisfactory. The experimental setup has the advantages of the two-dimensional detector transmission setup (Baerlocher *et al.*, 2004), but with better resolution in both d_{min} and FWHM. In contrast to the experiments with the Mythen I detector, all patterns are usually collected with counting statistics sufficient for intensity extraction. In order to satisfy the high photon flux requirements, a focused X-ray beam rather than a defocused one is used,[1] although the beam homogeneity suffers slightly.

Although this fact is well known for experts in texture analysis, it is worth mentioning for the general audience that the sample rotation φ and the tilt χ in transmission geometry do not correspond exactly to the reflection geometry angles (α, β) that are used in the texture analysis, so a conversion is necessary (Kocks *et al.*, 2000). As the Eulerian cradle is not tilted around ω ($\omega = 0°$), the conversion equation by Heidelbach *et al.* (1999) simplifies to

$$\cos\beta = \cos\theta\,|\cos\chi| \tag{1}$$

and the pole figure azimuth becomes

$$\alpha = \varphi - \arcsin(\sin\theta/\sin\chi). \tag{2}$$

[1] With the undulator installed in 2011, focusing is no longer necessary.

2.3. Mythen II microstrip detector

The improved one-dimensional Mythen II Si microstrip detector (Bergamaschi *et al.*, 2010) provides a larger dynamic and 2θ range than the prototype Mythen I detector (Schmitt *et al.*, 2004). It consists of 24 modules, each equipped with 1280 channels covering an angular range of 4.83°. This yields a step size of 0.0038° and, with the 0.17° gaps between the modules, an accessible 2θ range of 120°. To cover the 0.17° 2θ gaps between modules, at least two detector positions have to be used. A typical data set is measured for 5–10 s at each of 4–8 detector positions. Thus, the data collection for one sample measured at 302 different orientations φ/χ (see §2.6) including the mechanical movement of the Eulerian cradle and the detector takes from 2 to 8 h. Fig. 1 shows the angle convention for the SLS experimental setup.

2.4. Positive and negative 2θ range

The large 2θ range of the Mythen II detector (120° 2θ) offers the possibility of measuring both positive and negative 2θ angles (corresponding to $\eta = 90°$ and $\eta = 270°$, respectively) simultaneously: that is, two orientations can be measured to 60° 2θ ($d_{\min}$ = 1.0 Å for λ = 1.0 Å) at the same time. For a conventional powder X-ray diffraction (PXRD) measurement, the negative 2θ angles would not yield additional information, but for a textured sample the powder patterns are indeed different (see Fig. 3). The orientation of the negative 2θ pattern corresponds to a change in χ of 180° (for $\omega = 0$). Thus, the pole distance β does not change,

$$\begin{aligned}\cos\beta &= \cos\theta\,|\cos(\chi+\pi)| = \cos\theta\,|-\cos\chi| \\ &= \cos\theta\,|\cos\chi|, \end{aligned} \tag{3}$$

but the pole azimuth α becomes

$$\begin{aligned}\alpha &= \varphi - \arcsin[\sin\theta/\sin(\chi+\pi)] = \varphi - \arcsin(\sin\theta/-\sin\chi) \\ &= \varphi + \arcsin(\sin\theta/\sin\chi). \end{aligned} \tag{4}$$

The full rotation matrix converting instrumental and sample-related angles, which is applied in *MAUD*, is given in Appendix *A*.

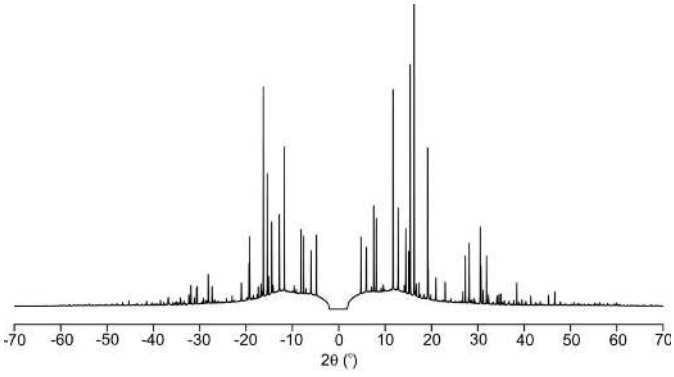

Figure 3
One $ZrPO_4$-pyr pattern ($\varphi = 65°/\chi = 320°$) with two orientations: one for $\eta = 270°$ (left) and one for $\eta = 90°$ (right).

2.5. Additional sample tilt angle

Part of the pole figure is not accessible in a conventional transmission mode experiment: that is, β angles below θ cannot be measured. By introducing an additional sample tilt angle ω, however, this region can be accessed. A simple test of this geometry using a goniometer head with an additional arc (change in ω of up to 80° possible) was performed, and the results are shown in Fig. 4. The experimental pole figures from two data collections of a textured sample of the niobium silicate AM-11 (Rocha *et al.*, 1998) with different ω tilts are shown. By merging data sets with different ω angles, the blind regions can be eliminated and the full (α, β) range of the pole figure accessed.

2.6. Optimized pole figure coverage

The number of measured orientations, and consequently the measuring time, can be reduced significantly by optimizing the pole figure coverage. In previous experiments, 1368 powder diffraction patterns were collected [5° steps in both φ (0–355°) and χ (270–360°)]. This was a requirement of the texture analysis programs that were available at the time. As can be seen in Fig. 5, much of the information at lower χ angles is redundant. This fixed-step format is not required by *MAUD*, so a set of orientations with optimized pole figure coverage can be selected for measurement. For the hexagonal

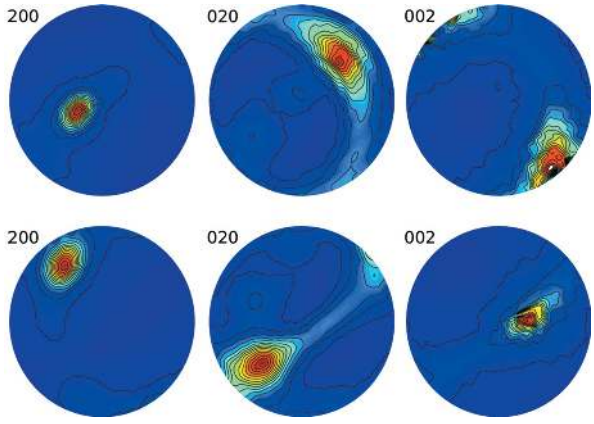

Figure 4
Experimental pole figures generated in *MAUD* for the orthorhombic niobium silicate AM-11 for $\omega = 0°$ (top) and $\omega = -80°$ (bottom). The missing information in the center of the pole figure ($\beta < \theta$) has been filled in by extrapolation by the program.

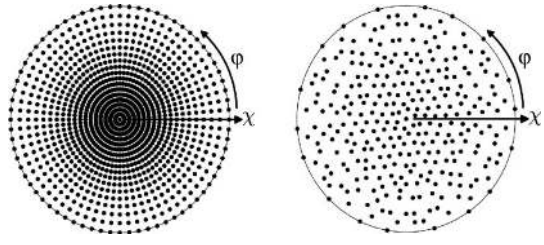

Figure 5
Pole figure showing the 1368 orientations measured in previous experiments (left) and the 302 orientations with optimized coverage measured with the new data collection strategy (right).

grid with 10° resolution that was used to select the orientations to be measured, only 302 orientations are required. The effect of using both data sets for $\eta = 90°$ and $\eta = 270°$ combined with optimized pole figure coverage is shown in Fig. 6.

3. Data analysis

Data analysis, which is performed using *MAUD*, involves two steps. First, a few non-overlapping reflections at low diffraction angles are selected to determine the orientation of the crystallites in the sample. This is done by computing their experimental pole figures (PFs, variation of intensity as a function of sample orientation) and calculating the corresponding orientation distribution function (ODF). This ODF is then used to calculate the pole figure values (P_{hkl}) for all reflections, and these are applied in a joint refinement of a set of powder patterns to obtain a single set of more single-crystal-like reflection intensities using equation (5):

$$y(2\theta, \varphi, \chi) = \sum_{hkl} I_{hkl}\, P_{hkl}(\varphi, \chi)\, G(2\theta - 2\theta_{hkl}), \qquad (5)$$

where y is the intensity observed at a specific 2θ angle and sample orientation (φ, χ), I_{hkl} is the single-crystal intensity, $P_{hkl}(\varphi, \chi)$ is the pole figure value, and G is the peak shape function.

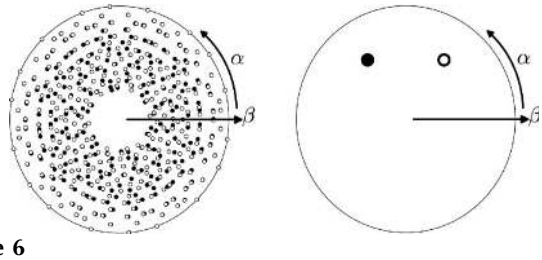

Figure 6
Pole figure coverage for $2\theta = 40°$. Orientations for $\eta = 90°$ are shown as filled circles and those for $\eta = 270°$ as open circles (left). In order to illustrate the effect of measuring two powder diffraction patterns for each sample orientation (φ, χ), the pole figure positions for a single sample orientation ($\varphi = 90°$, $\chi = 330°$) and the two detector positions, $\eta = 90°$ (filled) and $\eta = 270°$ (open), are shown separately (right).

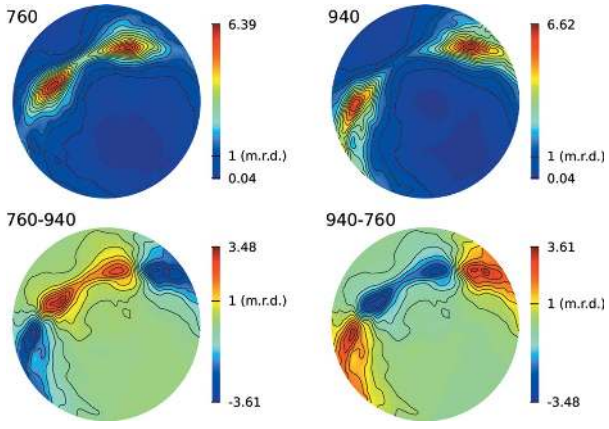

Figure 7
Pole figures calculated from the ODF for the overlapping reflections 760 and 940 in $ZrPO_4$-pyr (top), and the corresponding difference pole figures.

3.1. Raw data processing

The raw data from the detector are processed using the Fortran program *postpro_AC_0.3d* developed at SLS (Bergamaschi *et al.*, 2010). The routine converts detector channels to diffraction angles 2θ, merges data from several detector positions, performs a flat-field correction, eliminates dead/hot detector channels and normalizes the data to reflect any changes in the incident X-ray beam intensity. If the quality of the data in terms of counting statistics is low, a smoothing procedure can be applied. The latter is useful for beam-sensitive samples that must be measured quickly.

3.2. Orientation distribution function determination

To determine the orientation of the crystallites in the sample, all 302 measured powder patterns are imported into *MAUD*. Just a few strong and non-overlapping reflections at low 2θ angles (up to 15–20° 2θ for $\lambda = 1.0$ Å) are usually sufficient for this procedure, so only this section of the data needs to be processed at this stage. A simple algorithm performs the background subtraction with interpolation points. Then a Le Bail refinement (Matthies *et al.*, 1997) of all patterns is applied to optimize a set of unit cell and Popa (1998) line-broadening parameters and to extract the reflection intensities from the individual patterns. From these intensities, experimental pole figures are generated and used to compute the ODF using the extended WIMV method (Lutterotti, 2010), which was derived from the WIMV algorithm (Matthies & Vinel, 1982) but modified especially for the application of the Rietveld (1969) method.

3.3. Selection of the orientations for the joint refinement

The second step in the data analysis uses the texture information from the first step to extract more single-crystal-like intensities for the overlapping reflections. To do this, the patterns yielding maximum information about such reflections have to be selected.

A new strategy for this step has been developed. First, PFs for all reflections in the 2θ range that will be used for this second intensity extraction are calculated from the ODF in *BEARTEX* format (Wenk *et al.*, 1998). Second, difference PFs are calculated from these PFs for each group of overlapping reflections (example shown in Fig. 7). Those orientations that represent maxima in the PFs for non-overlapping reflections or maximum differences for overlapping reflections (texture contrast) are extracted. A weighting factor $1/(n-1)$ for each difference PF within an overlap group with n reflections is used to avoid overweighting reflections belonging to large overlap groups (*i.e.* contributing to a large number of difference PFs). Finally, those orientations with the largest number of (difference) PFs are selected and re-imported to *MAUD* for intensity extraction.

Fig. 8 shows a typical histogram indicating how the first orientation is selected by the program. The (difference) pole figures used in this step are then eliminated from the list and the procedure is repeated to select the second orientation *etc*. The amount of accessible information gained as a function of

the number of patterns (orientations) to be used in the intensity extraction is shown in Fig. 9.

For data sets with large overlap groups, the 2θ range might have to be limited for the computation [for each overlap group $n(n-1)$ difference PFs are generated]. It is expected that, even when some overlap groups are not included, a meaningful selection of orientations will result. The number of patterns required for the subsequent joint intensity extraction will vary depending on the strength of the texture. For the $ZrPO_4$-pyr example, eight patterns were sufficient to improve the reliability of extracted structure factors considerably over those obtained from conventional high-resolution powder diffraction data (see §4.3).

3.4. Joint extraction

The powder patterns selected for the intensity extraction have to be background corrected before being imported into *MAUD*. While the automatic background correction routine is sufficient to treat the background at low diffraction angles (for the ODF determination), the intensity extraction step requires a more sophisticated, individual background correction for each pattern. A program for this manual background treatment using linear interpolation or cubic splines has been written. It proved to be crucial to have a well estimated background for each pattern. With these background-corrected patterns and the ODF from the first step, a joint refinement using the full 2θ range for the selected orientations is performed to solve equation (5) for I_{hkl}. During the refinement procedure, the unit-cell parameters and the Popa parameters for line broadening and microstrain are optimized for all patterns simultaneously (Popa, 1998). However, the sample displacement parameters need to be optimized for each pattern individually. Minor misalignments of the sample with respect to the detector at different sample orientations cause shifts in 2θ that have to be corrected. The background and the texture are not refined during the joint extraction. The final set of I_{hkl} extracted in this way should fit all measured patterns, with the P_{hkl} values accounting for the differences in the measured intensities. The extracted structure factors can then be used as input to standard crystal structure determination programs. Data from a textured sample can also be combined with those from a conventional high-resolution PXRD experiment. The amplitudes from the texture method extraction should yield a more reliable partitioning of overlapping reflections and can be used as starting values for a refinement in a Le Bail extraction using conventionally collected powder diffraction data. This is because the sum of intensities within an overlap group can be expected to be measured more reliably in high-resolution powder diffraction data collected on an untextured sample.

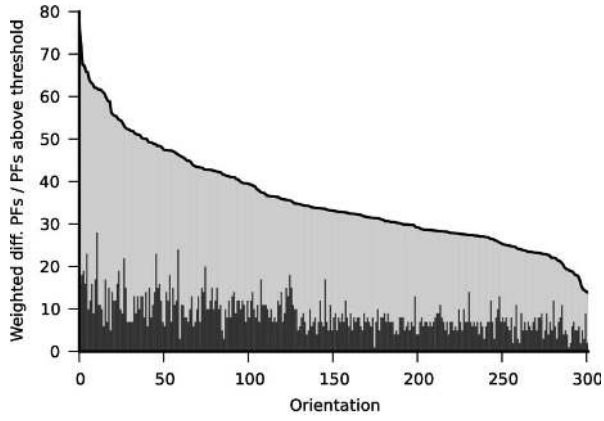

Figure 8
Histogram showing the result of the first cycle of the algorithm to choose the orientations for intensity extraction (the left-most orientation is selected). Reflections up to 60° 2θ were considered. The contribution from non-overlapping reflections is plotted in black and that from overlapping reflections in gray. Suitable orientations in the (difference) PF for this step were defined as those with $P \geq 0.66P_{max}$ and $P \geq 2.00$.

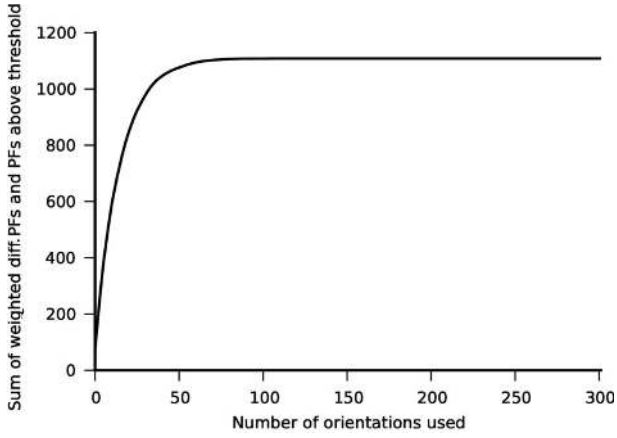

Figure 9
Plot of the amount of information gained as a function of the number of sample orientations included in the joint intensity extraction for $ZrPO_4$-pyr (reflections up to 60° 2θ considered).

Table 1
Data collection parameters for textured $ZrPO_4$-pyr.

Texture measurement, June 2010.

Synchrotron facility	Materials Science beamline, SLS, PSI
Sample	Textured, spherical, 0.4 mm
Wavelength (Å)	1.000
Range for ODF determination (° 2θ)	4.5–14.7
Range for joint extraction (° 2θ)	4.5–60.0
302 orientations in range of	
φ (°)	0–355
χ (°)	270–360
16 sample orientations (φ/χ) (°) used for intensity extraction	(190/290), (020/305), (150/315), (220/315), (185/320), (325/325), (090/330), (270/330), (265/340), (340/340), (250/345), (065/350), (290/350), (160/355), (245/360), (320/360)
Step size (° 2θ)	0.004
Detector positions	8
Time per pattern (s)	5

4. Test structure: zirconium phosphate pyridinium

In order to check the effect of the improvements outlined in the previous sections, two data sets of a zirconium phosphate framework material with a known structure ($ZrPO_4$-pyr), were collected using (1) a textured sample and the revised

experimental setup and data collection strategy, and (2) a conventional untextured sample in a 0.5 mm capillary. In the following sections, these two types of data will be referred to as TexDat and UntexDat, respectively. Both data sets were collected at the SLS with the Mythen II detector (see Tables 1 and 2 for details regarding the data collection). For the analysis, reflections up to a minimum d spacing of 1.0 Å were considered, and a reflection separation factor of 0.5 FWHM was used to define the overlap groups.

4.1. Sample preparation

Scanning electron microscopy images of $ZrPO_4$-pyr show needle-shaped crystals about 5 µm in length. Thus, the material appeared to be well suited for the preparation of a textured sample. Using the bakery folding method with a sample:polystyrene ratio of ∼1:2, a sample of *ca* 0.4 mm in diameter was prepared. The sample was screened using a single-crystal diffractometer to ensure that a suitable preferred orientation had been induced.

4.2. Data collection

An untextured sample of cubic zeolite A was measured at several orientations (φ, χ) to check the alignment of the Eulerian cradle and the beam homogeneity. Then 302 powder patterns of the textured $ZrPO_4$-pyr sample were collected using the strategy described in §2. Sections of three of these patterns exhibiting strong intensity contrast are shown in Fig. 10.

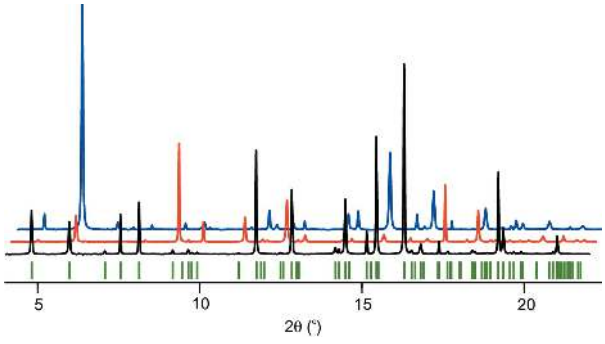

Figure 10
Sections of three powder patterns collected on $ZrPO_4$-pyr at different sample orientations φ/χ showing strong intensity differences [φ/χ = 150/315 (black), 270/330 (red) and 55/355 (blue)]. Tick marks indicate the positions of the reflections.

Table 2
Data collection parameters for untextured $ZrPO_4$-pyr.

Capillary measurement, October 2009.

Synchrotron facility	Materials Science beamline, SLS, PSI
Capillary diameter (mm)	0.5
Wavelength (Å)	1.000
Range (° 2θ)	4.0–100.0
Step size (° 2θ)	0.004
Detector positions	16
Time per pattern (s)	10

4.3. Data analysis

The raw data processing and the ODF determination in *MAUD* were performed as described in §3.1. The agreement between observed and recalculated pole figures was excellent (see Fig. 11). A threshold of 0.66 of the maximum P_{hkl} for each (difference) pole figure and an absolute minimum of $P_{hkl} \geq 1.50$ to consider an orientation as being suitable for a (difference) pole figure was used to select the patterns to be used for the intensity extraction. Fig. 12 shows the positions of these orientations (φ, χ) in a pole figure. Joint extractions using 8, 16 and 24 patterns were performed to test how many patterns would be necessary to obtain well resolved intensities for overlapping reflections. One refinement also uses UntexDat, but with starting values from TexDat with 16 powder patterns.

The comparison of the structure factors extracted from conventionally measured powder diffraction data with those derived from a textured sample indeed shows a significant improvement. The agreement between the amplitudes obtained in a Le Bail extraction for UntexDat and those calculated from the refined crystal structure can be expressed as an R value of 0.4679. For overlapping reflections only (80% of 1122 reflections) an R value of 0.5614 was obtained.

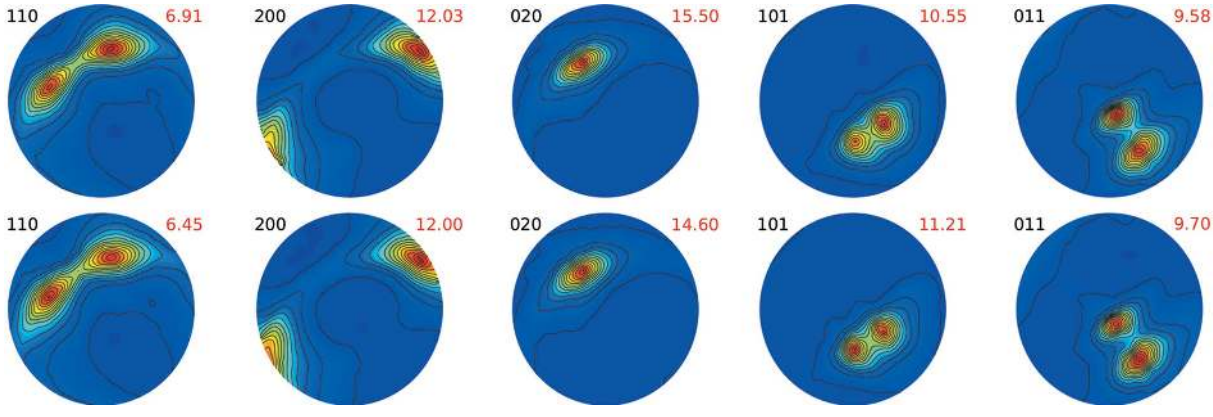

Figure 11
Experimental pole figures for $ZrPO_4$-pyr (top) and their counterparts reconstructed in *MAUD* from the ODF (bottom). The maximum P value for each pole figure is shown in red.

Amplitudes derived in a joint extraction using 16 powder patterns collected on a textured sample yielded R values of 0.2863 and 0.3189 for all and overlapping reflections (88% of 1122 reflections), respectively. The quality of the extraction could be further improved by combining the reflection partitioning from the textured sample with the amplitudes derived from UntexDat, which had better counting statistics, a more uniform background, slightly sharper peaks and therefore less overlap (80% instead of 88%). For this approach, the partitioning from TexDat provides starting values for a refinement with UntexDat. This combination results in R values of 0.2641 for all and 0.3066 for overlapping reflections (see Fig. 13). The quality of the intensities of non-overlapping reflections also improved with TexDat. These single reflections were expected to be more reliable for conventional PXRD data, but obviously the error in the P-value estimation for the textured sample was smaller than the deviation from ideal random distribution of the crystallites that was assumed for the untextured sample. This is perhaps not surprising for a material that contains needle-shaped crystallites (anisotropy in crystal morphology was a requirement for the sample preparation). Furthermore, a reflection separation factor of 0.5FWHM may be too optimistic for defining reflections as being completely separated. Fig. 14 shows the improvement in the reliability of the structure factors extracted from the data (F_{obs}) and those calculated from the known crystal structure (F_{calc}).

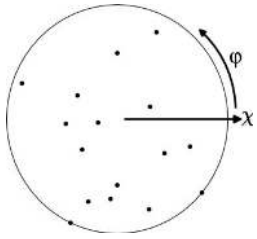

Figure 12
The 16 orientations used for the $ZrPO_4$-pyr intensity extraction.

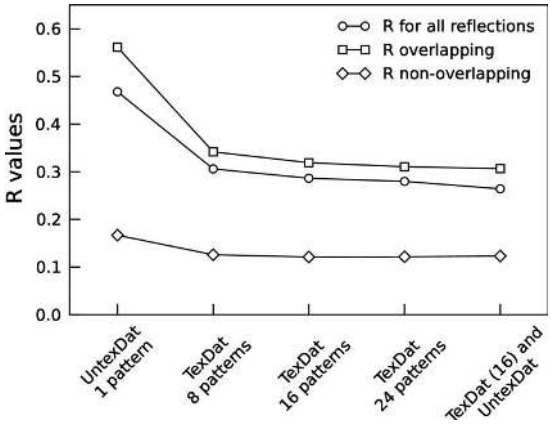

Figure 13
R values for the $ZrPO_4$-pyr intensities extracted from measurements on untextured and textured samples.

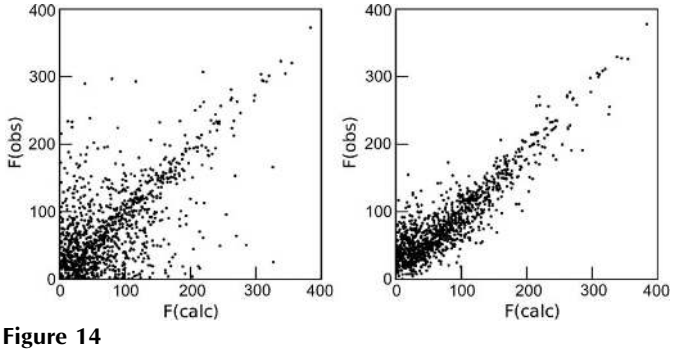

Figure 14
F_{calc} *versus* F_{obs} scatter plot for conventional PXRD data (R = 46.79%, left) and data from a textured sample using 16 patterns (R = 28.63%, right).

4.4. Discussion

Analysis of the $ZrPO_4$-pyr data shows that, with the latest experimental setup for the texture method, much more reliable structure factor amplitudes can be derived for reflections that overlap in a conventional powder diffraction pattern. In the example presented, a joint extraction using just eight patterns from a textured sample was sufficient to outperform a conventional powder diffraction data set by far. By combining texture-method and conventional PXRD data, even better estimates of the relative intensities of overlapping reflections could be obtained.

5. Conclusions

It has been shown that, with the modified experimental setup, textured samples can be measured to facilitate structure solution from powder diffraction data in a reasonable amount of time in an almost routine manner. The $ZrPO_4$-pyr example shows that the reliability of structure factor amplitudes derived from a textured sample are significantly improved over those obtained from conventional high-resolution powder diffraction data. This improvement should allow some crystal structures that are inaccessible with conventional powder diffraction data to be solved. Furthermore, as a result of the new features in the program *MAUD*, the data analysis procedure has been simplified to the point that the method can be used by non-experts.

APPENDIX *A*
Angle conversion between goniometer and pole figure space in *MAUD*

A sample reference coordinate system is defined by (X, Y, Z), and the instrument coordinate system by (X_i, Y_i, Z_i). $\mathbf{X}_i$ is defined as the direction of the incident beam pointing from source to sample, and $\mathbf{Z}_i$ is in the plane described by the incident beam and the diffracted beam, when the detector is placed in the 0° azimuthal (horizontal) position. This way, $\mathbf{Y}_i$ coincides with the rotation axis ω (or θ) of the goniometer. The goniometer measurement coordinates are described with three angles: ω, χ and φ. With an ω rotation around $\mathbf{Y}_i$ another

set of coordinates in the system (X_i', Y_i, Z_i') is generated, and χ is the rotation around $\mathbf{X}_i'$ (right-handed rotation considering the $\mathbf{X}_i'$ direction). With the χ rotation, a new set of coordinates in the system (X_i', Y_i', Z_i'') is generated and φ is the right-handed rotation around $\mathbf{Z}_i''$. At this point the sample reference (X, Y, Z) will be coincident with (X_i'', Y_i'', Z_i'').

By including the diffraction angle 2θ, the conversion from goniometer angles to pole figure angles (α, β) can be performed through the matrix of rotation M (capital Greek letters are the rotation matrices for the corresponding angles):

$$M = -\Theta\Omega\mathrm{X}\Phi. \tag{6}$$

If the diffraction point (detector position) is out of the usual (horizontal) 2θ diffraction circle, and η is the azimuthal angle of the detector (counterclockwise rotation), the new rotation matrix becomes

$$M = -\Theta\mathrm{H}\Omega\mathrm{X}\Phi. \tag{7}$$

Finally, if it is necessary to use a different coordinate system for the sample, which is not coincident with the instrument coordinate system for $\omega, \chi, \varphi = 0$, its orientation can be defined with similar angles $\omega_s, \chi_s, \varphi_s$ (same rotation axes at zero as ω, χ, φ). The final formula for the rotation matrix then becomes

$$M = -\Theta\mathrm{H}\Omega\mathrm{X}\Phi\Phi_s\mathrm{X}_s\Omega_s. \tag{8}$$

Thus, the pole figure angles are

$$\beta = \arccos(M_{33}), \tag{9}$$

$$\alpha = \begin{cases} 0, & \text{for } \beta = 0, \\ -\arctan(M_{31}/M_{32}), & \text{for } \beta \neq 0. \end{cases} \tag{10}$$

with M_{31}, M_{32}, M_{33} as third-row elements of the rotation matrix M.

The experimental assistance from the staff of the Materials Science beamline at the Swiss Light Source is gratefully acknowledged. This work was supported by the Swiss National Science Foundation.

References

Baerlocher, Ch., McCusker, L. B., Prokić, S. & Wessels, T. (2004). *Z. Kristallogr.* **219**, 803–812.

Bergamaschi, A., Cervellino, A., Dinapoli, R., Gozzo, F., Henrich, B., Johnson, I., Kraft, P., Mozzanica, A., Schmitt, B. & Shi, X. (2010). *J. Synchrotron Rad.* **17**, 653–668.

Dong, J., Liu, L., Li, J., Li, Y., Baerlocher, Ch. & McCusker, L. B. (2007). *Microporous Mesoporous Mater.* **104**, 185–191.

Estienne, C. (2008). *Preparation of Textured Samples by the Bakery Folding Method*. Internal Communication, ETH Zurich, Switzerland.

Hedel, R., Bunge, H. J. & Reck, G. (1997). *Textures Microstruct.* **29**, 103–126.

Heidelbach, F., Riekel, C. & Wenk, H.-R. (1999). *J. Appl. Cryst.* **32**, 841–849.

Kocks, U. F., Tomé, C. N. & Wenk, H.-R. (2000). *Texture and Anisotropy. Preferred Orientation in Polycrystals and their Effect on Material Properties*, 2nd ed., pp. 126–159. Cambridge University Press.

Lutterotti, L. (2010). *Nucl. Instrum. Methods Phys. Res. Sect. B*, **268**, 334–340.

Lutterotti, L., Matthies, S. & Wenk, H. R. (1999). *IUCr Commission on Powder Diffraction Newsletter*, No. 21, pp. 14–15.

Massüger, L. (2007). PhD thesis, ETH Zurich, Switzerland.

Matthies, S., Lutterotti, L. & Wenk, H. R. (1997). *J. Appl. Cryst.* **30**, 31–42.

Matthies, S. & Vinel, G. W. (1982). *Phys. Status Solidi B*, **112**, K111–K114.

Pecharsky, V. K. & Zavalij, P. Y. (2009). *Fundamentals of Powder Diffraction and Structural Characterization of Materials*, 2nd ed. pp. 497–544. New York: Springer.

Popa, N. C. (1998). *J. Appl. Cryst.* **31**, 176–180.

Prokić, S. (2004). PhD thesis, University of Zurich, Switzerland.

Rietveld, H. M. (1969). *J. Appl. Cryst.* **2**, 65–71.

Rocha, J., Brandao, P., Philippou, A. & Anderson, M. W. (1998). *Chem. Commun.* pp. 2687–2688.

Schmitt, B., Brönnimann, Ch., Eikenberry, E. F., Hülsen, G., Toyokawa, H., Horisberger, R., Gozzo, F., Patterson, B., Schulze-Briese, C. & Tomizaki, T. (2004). *Nucl. Instrum. Methods Phys. Res. Sect. A*, **518**, 436–439.

Wenk, H.-R., Matthies, S., Donovan, J. & Chateigner, D. (1998). *J. Appl. Cryst.* **31**, 262–269.

Wessels, T. (1999). PhD thesis, ETH Zurich, Switzerland.

Wessels, T., Baerlocher, C. & McCusker, L. B. (1999). *Science*, **284**, 477–479.